

## Article

# Rock Physical Properties of Longmaxi Shale Gas Formation in South Sichuan Province, China

Wei Guo <sup>1</sup>, Majia Zheng <sup>2</sup>, Zhonghua Liu <sup>1</sup>, Weijun Shen <sup>3,\*</sup>, Shangwen Zhou <sup>1</sup>, Pingping Liang <sup>1</sup> and Yuchuan Chen <sup>4,\*</sup>

<sup>1</sup> Research Institute of Petroleum Exploration and Development, PetroChina, Beijing 100020, China

<sup>2</sup> Southern Sichuan Gas District of PetroChina Southwest Oil & Gasfield Company, Luzhou 646000, China

<sup>3</sup> Key Laboratory for Mechanics in Fluid Solid Coupling Systems, Institute of Mechanics, Chinese Academy of Sciences, Beijing 100190, China

<sup>4</sup> School of Geosciences, Yangtze University, Wuhan 430100, China

\* Correspondence: wjshen763@imech.ac.cn (W.S.); 2021710374@yangtzeu.edu.cn (Y.C.); Tel.: +86-010-82544017 (W.S.)

**Abstract:** Deep shale gas (burial depth > 3500 m) in the Longmaxi Formation of southern Sichuan Province will be the primary target for exploration and development in China for a relatively long period. However, the lack of a physical basis for the “sweet-spots” seismic and well-logging prediction is caused by uncertainty in the rock physical properties of deep shale gas in the research area. Acoustic and hardness measurements were performed on shale samples from a deep layer of the Longmaxi Formation in southern Sichuan. Microtextural characteristics of the shale samples were also analyzed by conventional optical microscopy and scanning electron microscopy. Based on these measurements, the rock physical properties of the shale samples and control factors are discussed. It is shown that the deep shale samples have similar properties to the shallow shale in mineral composition, microtexture, and pore type. However, the organic pore in deep shale samples is relatively undeveloped, while the dissolved pores are more developed. For high-quality shale samples (total organic content > 2%), crystal quartz of biological origin forms the framework of rock samples, resulting in effective dynamic and static properties, reflecting the elastic behavior of rigid quartz aggregates. For organic-lean samples (total organic content < 2%), orientated detrital clay particles take the role of load-bearing grains. Therefore, these shale samples’ overall rock physical properties are mainly controlled by the elastic properties of “soft” clay. The load-bearing grain variation from organic-rich shale samples to organic-lean samples results in an overturned “V”-type change in terms of velocity versus content. Organic-rich shale samples also show an apparent low Poisson’s ratio. Organic-rich shale has a slight velocity–porosity trend, while organic-lean shale shows a significant velocity–porosity trend. In addition, due to the difference in rock microtexture between organic-rich and organic-lean shale, these two kinds of reservoir rocks can be discriminated in cross plots of P-wave impedance versus Poisson’s ratio and Young’s modulus versus Poisson’s ratio. Change in hardness also reflects the control of microtexture, and shale samples with biological-origin quartz as load-bearing grains show higher hardness and brittleness. However, the variation in quartz content has less of an impact on hardness and brittleness in shale samples with clay as the load-bearing grain. Our results provide an experimental basis for the geophysical identification and prediction of deep shale gas layers.



**Citation:** Guo, W.; Zheng, M.; Liu, Z.; Shen, W.; Zhou, S.; Liang, P.; Chen, Y. Rock Physical Properties of Longmaxi Shale Gas Formation in South Sichuan Province, China. *Minerals* **2023**, *13*, 485. <https://doi.org/10.3390/min13040485>

Academic Editor: Thomas Gentzis

Received: 24 November 2022

Revised: 25 March 2023

Accepted: 27 March 2023

Published: 30 March 2023



**Copyright:** © 2023 by the authors. Licensee MDPI, Basel, Switzerland. This article is an open access article distributed under the terms and conditions of the Creative Commons Attribution (CC BY) license (<https://creativecommons.org/licenses/by/4.0/>).

**Keywords:** deep Longmaxi Formation shales; acoustic properties; geomechanical properties; velocity; hardness

## 1. Introduction

With increasing energy demand, unconventional shale gas has become the oil and gas resource of major concern in China. The Sichuan Basin and the Silurian Longmaxi Formation around it have been recognized as the headstream of black shale gas exploration

and development in China because of its rich organic matter, suitable burial depth, and high organic matter maturity. In the Fuling Jiaoshiba area and the Weiyuan–Changning block in Sichuan Province, Sinopec and PetroChina have made strides in this position since 2009, significantly promoting the commercial exploitation of shale gas in China [1–3].

The most direct and effective method for evaluating and predicting favorable shale gas blocks is seismic technology [4]; for instance, using seismic data in the exploration stage to predict the pattern of the shale gas layer (burial depth, thickness, and structure), the prestack and poststack inversion techniques to determine the characteristics of shale gas reservoir (organic matter content, porosity, mineral composition, total gas content, etc.), and the seismic techniques to determine the reservoir's anisotropic characteristics, seismic elastic characteristics, brittleness characteristics, and in situ stress to present the rules for the horizontal wellbore design and fracturing transformation. Through seismic attributes, the shaly petrophysical characteristics provide a direct link for obtaining the reservoir parameters and mechanical characteristics of shale gas reservoirs. Research globally on the change rules and influencing factors of the seismic elastic properties of shale has been conducted chiefly through systematic rock physics tests and using the quantitative seismic rock physics model. China prospected for shale gas later than other countries where studies on experimental rock physical properties of shale gas reservoirs are systematic. Representative shale experiments include that of Vernik and Nur (1992, 1997) [5,6], who used experimental results to determine the anisotropic properties of Bakken shale. They then examined the effects of organic matter content and maturity on the characteristics of rock speed and anisotropy. They noted that the anisotropy of shale was dependent on the preferred direction of clay minerals and microcracks [5–7]. Moreover, Sondergeld and Cai (2000, 2010) [8,9] studied the dynamic elastic properties of Kimmeridge shale and determined that shale anisotropy enlarged with increasing organic matter content.

In contrast, the increase in organic matter content would decrease bulk density and produce the opposite effect of compaction [8,9]. Therefore, the hypothesis of weak anisotropy could not be used in seismic velocity analysis and migration imaging of shale reservoirs. Dewhurst (2011) studied the effects of organic matter maturity and principal stress direction on shale anisotropy [10]. Based on microtexture observation and acoustic experiments, Deng Jixin et al. (2015, 2018) discovered the law of change in the dynamic elastic characteristics of the Longmaxi shale sample. They analyzed the ways in which the difference in deposition and diagenesis influenced the dynamic elastic properties of Longmaxi shale [11,12]. The results indicated that the shale at different regions and positions (depths) varied greatly in seismic elastic properties and was subject to the combined effects of organic matter (TOC; total organic content), pore characteristics, composition characteristics, rock structures, and reservoir conditions. The research work is also systematical in terms of the petrophysical model for quantitative expression of seismic elastic properties. For instance, an anisotropic self-consistent model and differential equation equivalent modulus formula were used to calculate the model of seismic elastic anisotropy, which discusses the effects of clay, TOC, and pore structure distribution characteristics on seismic elastic properties [13–15]. Guo Zhiqi et al. (2013) discovered a relationship between reservoir parameters, such as TOC, brittle minerals, and the seismic velocity anisotropy of shale, according to the spatial occurrence state of organic matter, pores, and primary mineral compositions [16]. Zhang Feng and Li et al. (2017) established a theoretical rock physical model of organic-rich shale by combining the SCA (self-consistent) and differential effective medium models to discuss the influence of pore geometry and mineral component on the seismic nature of shale [17].

The preceding shale experiment and petrophysical model research have supported the “Dessert” earthquake forecasting technology of shale reservoirs at the current stage. However, it should also be noted that due to the constraints of shale gas techniques of horizontal drilling and hydraulic fracturing, as well as economic benefits, studies on the seismic rock physical properties of shale gas reservoirs are concentrated on middle–shallow shale gas reservoirs with burial depth < 3500 m. In contrast, the Longmaxi shale layer in the Sichuan Basin is massively distributed in deep and ultradeep reservoirs. Take the

main exploration and development block of Longmaxi shale within the southern Sichuan's Weiyuan–Changning area as an example; the favorable exploration area of middle-shallow shale is 2500 km<sup>2</sup>. In contrast, the workable area of deep shale (deeper than 3500 m) comes up to 17,450 km<sup>2</sup> (provided by the Sichuan Basin Center of Research Institute of Petroleum Exploration and Development). The difference in the depth of Longmaxi shale will further lead to rock differences in the environment, sedimentation and diagenesis, and thermal evolution processes. Furthermore, the petrophysical experiment results indicate that seismic rock physics of middle–shallow shale are different and cannot be extrapolated at will. Therefore, the demand for the geophysical identification and prediction of deep shale gas layers requires systematic experimental research on the seismic rock physical properties of deep shale in the target area. Herein, systematic acoustic measurement, petrophysical properties, and rock microstructure of Longmaxi deep-shale samples were investigated, and the essential seismic petrophysical characteristics and change rule were summarized, helping explain the well logging of deep shale reservoirs in Longmaxi Formation and realize seismic “dessert” prediction.

## 2. Geological Background and Testing Methods

Shale samples (including Wufeng Formation shale samples) were obtained from four wells, including W106 in the Longmaxi Formation within the Weiyuan–Changning block. The research area is at the intersection of the ancient-fold diagonal gentle zone in middle Sichuan Province, the ancient diagonal slope-low-fold zone in southwest Sichuan, and the ancient-break median-fold low and precipitous curved zone in south Sichuan. In this area, the structure is gentle and simple, and the stratum exceeds the pressure at large (measured pressure coefficient: 1.99–2.25); the shale of Longmaxi Formation is well preserved with a burial depth of more than 3700 m, which belongs to a typical case of deep shale gas reservoir; the layers are fractionated into Long 2, Long 1-4, Long 1-3, Long 1-2, and Long 1-1 sublayer segments in terms of depth according to the depositional environment, components, deposition rate, organic matter content, and fossil type (provided by the Sichuan Basin Center of Research Institute of Petroleum Exploration and Development).

One hundred and twenty-one plunger samples (mainly cored in the direction vertical to bedding) were drilled in the four wells, covering four sublayer segments of the Longmaxi Formation shale. Samples represent volumetrically dominant lithofacies of the Longmaxi Formation shale. Visible irregularities, such as fractured surfaces, were avoided in sampling to minimize sources of uncertainty in analyses of subsamples. Each sample showed subtle variation in texture and composition, given the relatively thin scale of bedding and lamination relative to the sampling horizon. All cores were 25.4 mm in diameter and higher than 70 mm and further divided into 40–55 mm high plunger samples with an inclination of less than 0.05 mm to conduct acoustic, petrophysical, and mechanical property tests. Cores were also systematically subsampled for compositional, pore structure, and microstructural analysis. Inhibitive potassium-rich fluids (light mineral oil) were deployed as cooling fluids during drilling to lessen reactions between water and clay minerals [18]. All samples were oven-dried by heating up to a maximum temperature of 80 °C until the loss of sample weight leveled off to minimize potential alteration. This process allowed for water retention in pore spaces between clay platelets. Dry conditions in this report refer to ambient conditions for ultrasonic velocity measurements, which assume no free water in the pore spaces. Subparallel to bedding, microfractures form as a consequence of stress release after coring or from the expulsion of hydrocarbons. These microfractures influence the velocity and anisotropy of the rock, especially at low confining pressures [6,19,20].

The exact mineral compositions of the samples were determined by powder XRD (X-ray diffraction) analysis and pyrolysis. These procedures were conducted to analyze crushed sample powders (grain sizes < 48 µm) using a PANalytical (Empyrean) X-ray diffractometer. Whole rock geochemical analyses were conducted on samples by inductively coupled plasma-mass spectrometry (ICP-MS). These analytical methods yielded data for 13 major oxides and 10 trace elements. Calibration of analytical results was conducted

following internal laboratory standards. Total organic content (TOC) was also measured for samples using standard high-temperature pyrolyzation methods and A Leco carbon/sulfur analyzer. Using a Zeiss optical microscope and microphotometer, thermal maturity ( $Ro$ ) was estimated, and it was the solid bitumen. The lack of vitrinite in the Longmaxi Formation shales required the conversion of vitrinite-like maceral material reflectance ( $Rom$ ) to equivalent vitrinite reflectance ( $Ro$ ) using the equation obtained by Schoenherr (2007) [21]:

$$Ro = (Rom + 0.2443)/1.0495. \quad (1)$$

Focused ion beam scanning electron microscopy (FIB-SEM), scanning electron microscopy (SEM), and conventional optical microscopy were used to image and interpret the predominant microtextural character of samples, especially in terms of microcrystalline quartz. Argon (Ar)-ion polished thin sections of typical shale samples were examined by FIB-SEM (FEI Helios 650) with a backscattered electron (BSE) detector adapted for microtexture imaging at 4 nm pixel resolution. Samples were prepared with an Ar-ion thin section polisher operated at 5 kV and 100  $\mu$ A over a 10 h preparation period. The polished surface was then plasma-coated with a 10 nm thick gold film to enhance conductivity.

The sample's compressional and shear wave velocities were measured following the ultrasonic pulse transmission method. The compressional and shear velocity measurements' central frequencies were 800 and 350 kHz, respectively. Velocity measurements were conducted under the effective pressure of 40 MPa, approximately equal to the effective pressure under in situ conditions. Experiments began within a pressure cell at room temperature and confining pressures of 2 MPa, which ran up to 40 MPa in 5 MPa increments. Changes in sample length were monitored with pressure using axial gauges (length gauges). Velocities were calculated from the actual sample length by considering the viscoelastic relaxation deformation at each pressure step. For each pressure interval, the first break of the transmitted pulse was selected from a 20 min period during which the sample strain fell below  $2 \times 10^{-4}$ . This technique provided velocity measurements of approximately  $\pm 1\%$  for the compressional wave and approximately  $\pm 2\%$  for shear waves (Table A1 for the measurement results of 10 samples). Deviations in pressure were less than 0.3%. Boolean hardness was measured shortly after the dynamic elasticity test.

The Boyle–Mariotte Law was used to develop a method for calculating total porosity. This method uses grain and bulk volume estimates from a helium pycnometer under ambient conditions to calculate porosity from differences between bulk and grain volume. This approach provides porosity estimates only of connected pores in the samples.

### 3. Petrologic and Geochemical Characteristics of the Sample

Shale in the research area has been classified by a ternary diagram of siliceous mineral—carbonate mineral—clay mineral [22,23]. The organic-lean shale samples with less than 2% organic matter (TOC) are located in Long 2, Long 1-4, and Long 1-3 sublayers, mostly siliceous argillaceous shale, plus a small part of mixed siliceous shale (Figure 1); the average contents of felsic minerals, argillaceous minerals, and carbonate minerals are 35.7%, 51.6%, and 2.8% respectively; the average value of organic matter (TOC) is 0.96%, and the organic matter (TOC) content is greater than 2% of organic-rich shale samples that are primarily located in Long 1-2 and 1-1 sublayers where argillaceous siliceous shale and mixed shale are the main part, along with a small amount of grapholith. The average contents of argillaceous, siliceous, and carbonate minerals are 42.8%, 42.5%, and 12.1%, respectively, and the TOC averages 3.31%. Different types of lithofacies indicate different sedimentary environments. Siliceous shale facies are rich in organic matter such as algae and radiolaria. The development of pyrite reveals an anoxic reducing environment. The organic carbon and silica levels are low in siliceous clay shale facies, suggesting oxidation-weak reduction dominated the deposition environment. In the deep layer of organic-rich shale (Long 1-2, Long 1-1, TOC > 2%), the primary mineral compositions are the same as these of middle–shallow organic-rich shale in the Longmaxi Formation in the same research area; in other words, both are silicon-rich.

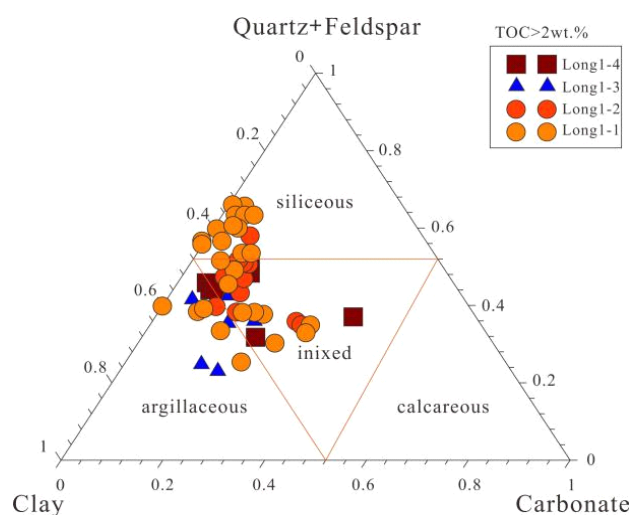


**Figure 1.** Ternary diagrams showing the mineral composition of the investigated samples. (Siliceous, mixed, calcareous, argillaceous shale facies.)

Deep shale samples exhibit the following types of porosity: intergranular, intercrys-tallite, organic, and fracture pores, to name a few, same as that of middle and shallow samples, but the pore development of deep shale organics is low, while the dissolved pores of samples with higher quality contents increase obviously (Figure 2b,e). Herein, samples in organic-lean shale reservoirs (Long 1-3, Long 1-4, Long 2) and organic-rich shale reservoirs (Long 1-1, Long 1-2) indicate significant changes in structural features and the compaction effect of Long 1-3, Long 1-4, and Long 2 shale samples are strong. Plastic particles, such as clay, deform remarkably around rigid quartz particles to “enfold” quartz particles and calcium particles, showing a strong clay orientation feature, forming an architectural system that uses clay as a matrix to support the particles (Figure 2a–c). TOC exists between the intergranular pores of the clay. In contrast, the pores are located between the elongated and flaky clay particles (Figure 2c), which are a kind of typical soft pores with respect to mechanical properties. Long 1-1 and Long 1-2 shale samples contain large amounts of microcrystalline silica particles in point and line contacts, randomly filled with exfoliated clay particles, resulting in weak directional characteristics. In rock structure, the microcrystalline silica particles make up a rock stress matrix (Figure 2d–f); the organic matter (TOC) mainly occurs between intergranular quartz pores and is not used as a stress matrix; the intergranular pores take a multilateral or triangular shape (Figure 2f) under the compaction and agglutination effects in the later period and show the features of hard pores with respect to mechanical properties.

The content of major elements plays an essential role in determining siliceous composition origin. Silicon of different origins often shows different chemical characteristics, and biogenetic siliceous shale contains large amounts of  $\text{SiO}_2$ ,  $\text{P}_2\text{O}_5$ , and  $\text{Fe}_2\text{O}_3$ , while the content of  $\text{Al}_2\text{O}_3$ ,  $\text{TiO}_2$ ,  $\text{FeO}$ , and  $\text{MgO}$  is comparatively low. The accumulation of Fe and Mn elements is mainly the result of hot water, while Al is associated with terrigenous clasts [24]. Samples,  $\text{Al}_2\text{O}_3$  and  $\text{TiO}_2$ , have a high correlation (Figure 3a), and the  $\text{Al}_2\text{O}_3$  and  $\text{TiO}_2$  contents of organic-rich shale samples are relatively low (not more than 9.14% and 0.45% in most of the samples), but there is no correlation with the content of  $\text{SiO}_2$  (Figure 3b,c). There is a noticeable distinction in  $\text{Al}_2\text{O}_3$  and  $\text{TiO}_2$  contents between organic-lean and organic-rich shale layers. This suggests that the two layers differ significantly in siliceous source and terrigenous matter contributes little to siliceous compositions. The  $\text{Si}/(\text{Si} + \text{Al} + \text{Fe})$  ratio is also an essential index for determining the origin of silicon, and the  $\text{Si}/(\text{Si} + \text{Al} + \text{Fe})$  ratio is generally higher than 0.9 for the biogenic siliceous rock [25]. The  $\text{Si}/(\text{Si} + \text{Al} + \text{Fe})$  ratio of organic-rich samples ranges from 0.9 to 0.93, indicating that the sample's quartz is chiefly of biogenic origin.

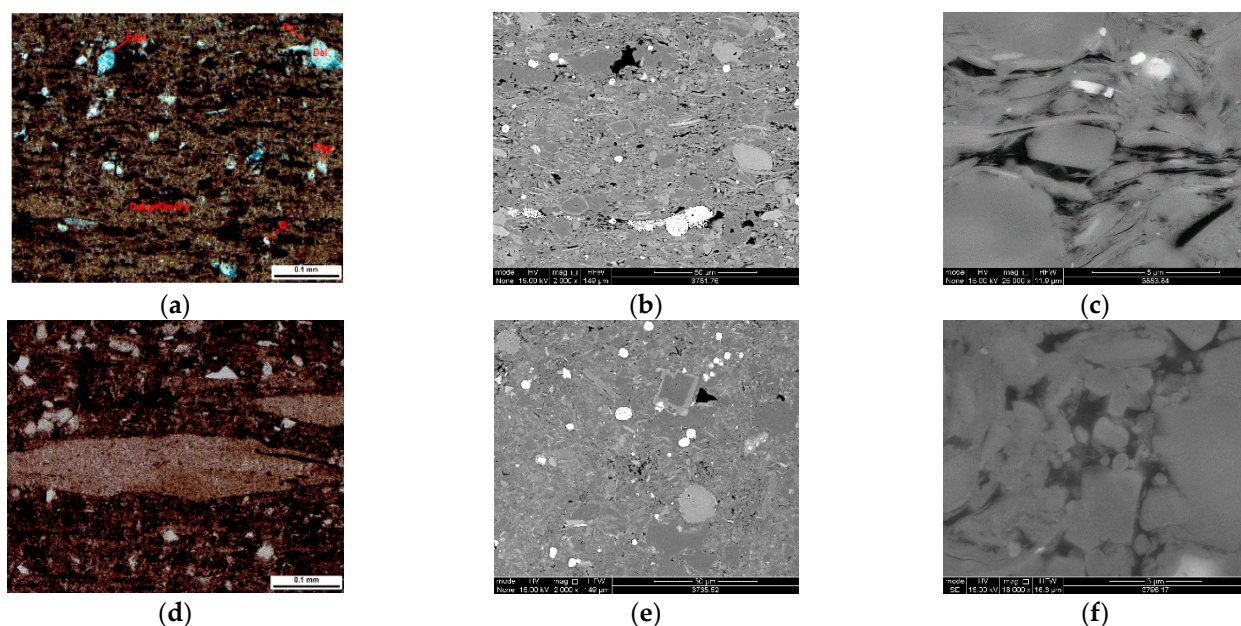


**Figure 2.** Examples of microtexture pore structures observed in thin sections and SEM images of deep Wufeng and Longmaxi Formation shales. (a) Preferential alignment of clay in organic-lean shale sample; (b) BEM photomicrographs of typical organic-lean sample; (c) pore and organic matter in organic-lean samples; (d) thin section imaging for organic-rich sample; (e) BEM photomicrographs in a typical organic-rich sample; (f) pore and organic matter in organic-rich samples.

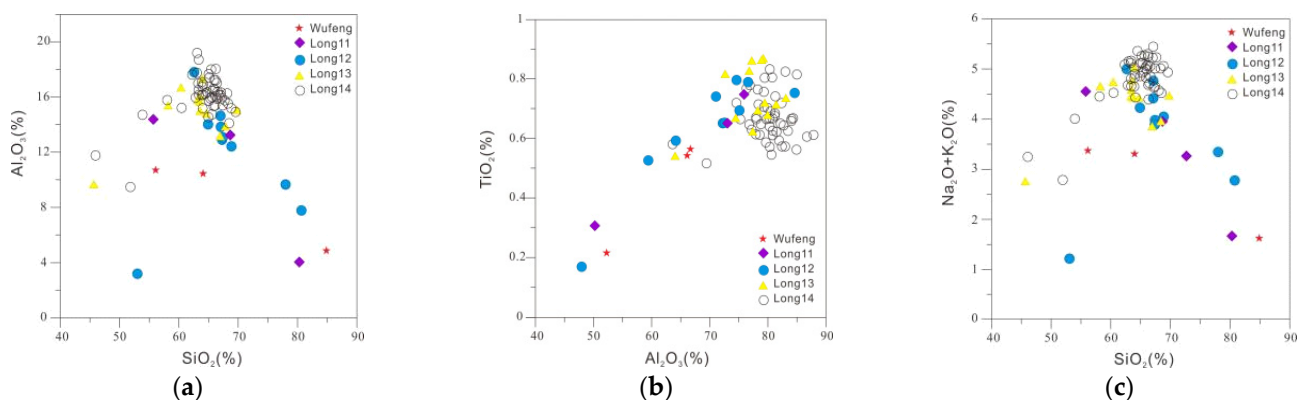


**Figure 3.** Relative proportions of  $\text{SiO}_2$ ,  $\text{Al}_2\text{O}_3$ , and  $\text{TiO}_2$  of the shale samples. (a) Relationship between  $\text{Al}_2\text{O}_3$  and  $\text{SiO}_2$ ; (b) relationship between  $\text{TiO}_2$  and  $\text{Al}_2\text{O}_3$ ; (c) relationship between  $\text{SiO}_2$  and  $\text{Na}_2\text{O} + \text{K}_2\text{O}$ .

The local siliceous content of the Longmaxi (Formation) shale is fairly high, and the  $\text{Si}/\text{Al}$  value is large. Above the illite,  $\text{Si}/\text{Al}$  line (fitted from the Si and Al contents in the Barnett clay shale) is the excess silicon portion, representing biogenic silicon [26]. As shown in Figure 4, the part above the illite  $\text{Si}/\text{Al}$  line consists of Long 1-1 and 1-2 organic-rich shale samples, indicating that the biogenic silicon is the primary element of the quartz in this layer, but the silicon origin of Long 1-1 shale varies in different wells, i.e., samples in well 131, which are primarily distributed below the illite  $\text{Si}/\text{Al}$  line, featuring terrigenous quartz, which differs remarkably from well 106 and R133, indicate source (silicon origin) unevenness in lateral variations of deep shale samples (Figure 4). Zirconium can also be used to trace the origin of quartz in shale samples, and it is mainly present in zircon-type heavy mineral assemblages to represent terrestrial detrital quartz [27]. The positive relationship between zirconium and quartz ( $\text{SiO}_2$ ) content reveals the contribution of terrestrial quartz to the silicon in the rock. In contrast, the negative relationship between

the two elements manifests the contribution made by the biogenic quartz to the silicon in the rock. The two experimental samples present an inverted “V” change feature (Figure 5). When the quartz content is less than 41%, zirconium and quartz show a positive relationship, primarily corresponding to organic-lean reservoir samples (Long 1-3, Long 1-4, and Long 2) and a few Long 1-1 and 1-2 samples, which indicate that the main elements are terrestrial clastic quartz. When the quartz content is more than 41%, zirconium and quartz show a negative relationship, predominated by organic-rich Long 1-1 and Long 1-2 samples, demonstrating that the quartz is of a biological origin. It also differs significantly in Long 1-1 shale samples in different wells.

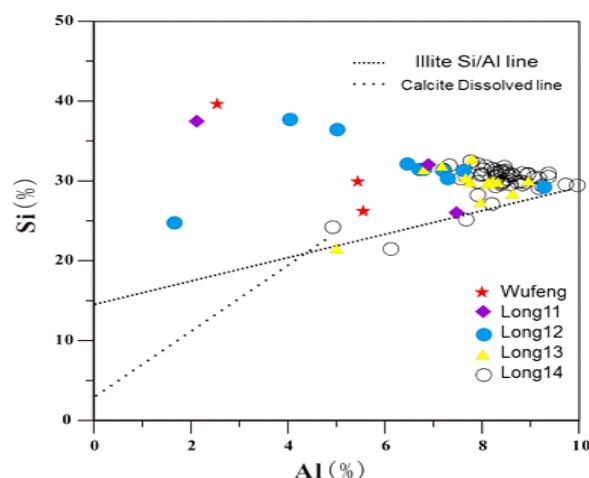


**Figure 4.** Relative cross-plots Si and Al compositions of all shale samples.

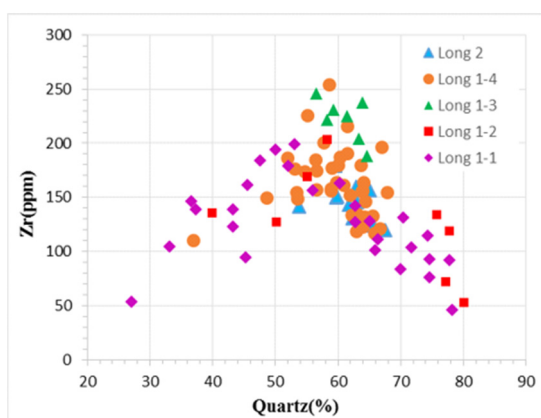


**Figure 5.** Cross-plots Zr and SiO<sub>2</sub> compositions of all shale samples.

The siliceous source has an important influence on the diagenesis of Longmaxi shale. The biological source of siliceous components represents the prosperity of organisms such as plankton and benthos fauna. In addition, it shows that the primary productivity in water bodies reaches a higher level, causing growth in TOC. The decomposition of considerable siliceous biologically makes the seawater silicon-enriched. When the silicon reaches a specific concentration, it is gradually precipitated to form a large amount of biogenic amorphous SiO<sub>2</sub>. With increasing burial depth, the reservoir temperature rises, and amorphous SiO<sub>2</sub> changes spontaneously from opal A to opal CT to compact microcrystalline quartz aggregates, forming a rock structure with the aggregates of microcrystalline quartz as a stress matrix. Early agglutination of microcrystalline quartz strengthens the rigidity of the rock matrix to weaken the impact of mechanical compaction, reduce the orientation of clay particles, and maintain the primary intergranular pores, which is beneficial to the occurrence of organic matter. Siliceous biolysis causes seawater supersaturation, and the high-silicon saturation enhances the stability of montmorillonite to hinder the conversion

of illite or its mixed-layer minerals. Therefore, the biogenic quartz and its agglutination effect should be earlier than those from the conversion of montmorillonite to illite. Thus, the organic-rich shale samples (Long 1-1 and Long 1-2) dominated by biogenic quartz feature microcrystalline quartz particles constituted rock matrix and high TOC. In terrestrial quartz-dominated shale layers (Long 1-3, Long 1-4, and Long 2), there is no early siliceous cementation, and the clay particles are rotating and arranged in a fixed direction under the overlying pressure in the mechanical compaction stage to form a rock matrix. Thus, the shale layers (Long 1-3, Long 1-4, and Long 2), which are rich in terrestrial quartz, are organic-lean reservoirs supported by clay particles and featured by low TOC.

#### 4. Rock Physical Properties of Shales

##### 4.1. Variety of Petrophysical Properties

Figure 6a demonstrates the correlation between TOC and quartz content of the organic-rich shale samples with more than 2% of TOC. The TOC increases as the silica content increases. Of the organic-lean samples ( $\text{TOC} < 2\%$ ), there is no apparent correlation between the two. The quartz content, especially biogenic quartz, indicates the primary productivity of paleoceanographic organic matter (TOC). Biogenic quartz can play a role in early cementing to improve the rigidity (pressure resistance) of the sediment aggregation, allowing the primary intergranular pores to be preserved, which has helped improve the preservation rate of organic matter. Therefore, a good coupling relationship is formed between the quartz content and the TOC. However, due to the nonuniformity of organic-rich reservoirs (Long 1-1 and Long 1-2), a few samples are still dominated by terrestrial quartz, resulting in low TOC. Figure 6b describes the relationship of shale sample porosity varying with TOC, both showing a weak positive correlation. The porosity change range in organic-rich and organic-lean reservoirs is 4%–8.7%. The nonreservoir shales also have high porosity. In shallow shale, the porosity of organic-rich shale with high TOC does not exceed 5%, and that with low TOC is usually approximately 2%. Simultaneously, for organic-rich shale (lower segment of Longmaxi Formation), the developed organic matter pores cause the porosity and TOC to show an obvious positive relation. In shallow shale (especially with high TOC), the organic matter pores significantly contribute to the total porosity of the shale. Conversely, the organic matter pores are less developed in deep shale. Moreover, as the dissolved pores are well developed due to an increase in burial depth, there is a visible difference in the change rule of porosity between shallow and deep shale.

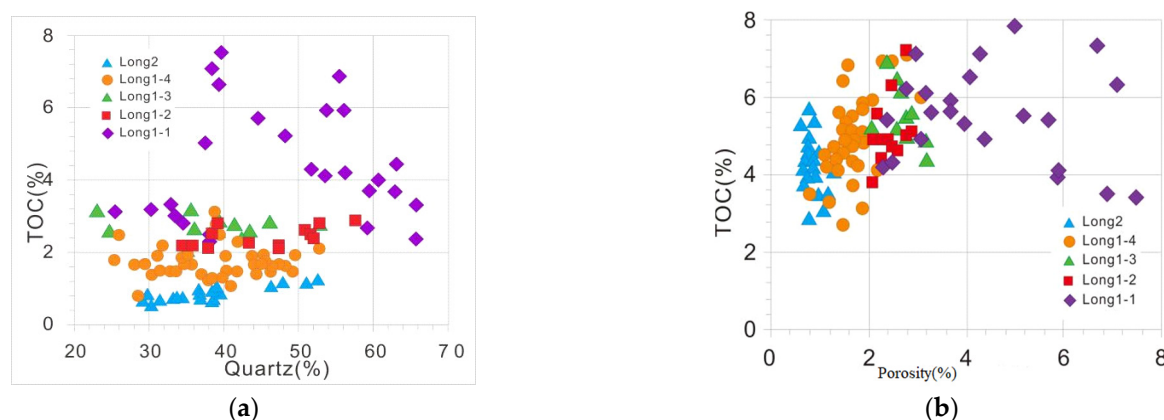


**Figure 6.** Relationship between TOC and quartz content. (a) Relationship between TOC and porosity (b) of the shale samples.

##### 4.2. Variety of Acoustic Velocity

Figure 7 shows the effect of quartz content in shale samples on compressional (P-wave velocity) and shear velocities (S-wave velocity) on the vertical bedding at an effective pressure of 40 MPa (approximately equal to the effective pressure of the stratum, see

Table A1 for velocity results). The figure shows that as the silica content increases, the velocity change in the shale sample presents an approximate asymmetrical inverted “V” trend (in the black arrow direction), i.e., P-wave velocity and S-wave velocity increase quickly as the quartz content reaches a certain amount. Further, it slows down as the quartz content keeps growing, and a (impedance) turning point appears when the quartz content is at about 41%. In Figures 4 and 7, we can observe that the change pattern of the velocity of quartz content is identical to that of trace element zirconia of silica content. The limit of 41% quartz content signifies that the samples are dominated by terrestrial detrital quartz or biogenic quartz, wherein clay particles back the former while the latter is of microcrystalline quartz. The change in the texture features of shale samples determines the overall varying velocity mode (quartz content). When the quartz content is less than 41%, “soft” clay particles serve as the rock matrix (Figure 2a–c), and the increase in quartz content will not change the load-bearing feature of the rock. The acoustic properties of the rock matrix are mainly controlled by the elastic properties of the load-bearing mineral-clay particles, resulting in a decrease in the sample shear velocity (Figure 7b). The variation in P- and S-wave velocities with quartz content occurs due to the decline in porosity and TOC (Figure 8a,b). Still, the lowering trend of porosity is obviously different from the variety of porosity during the conventional mudstone → sandstone mudstone process, wherein the former is caused by the gradual reduction in calcium content-related dissolved porosity and TOC, featuring low velocity samples corresponding to high calcium content and high porosity and high velocity samples corresponding to low calcium content and low porosity.

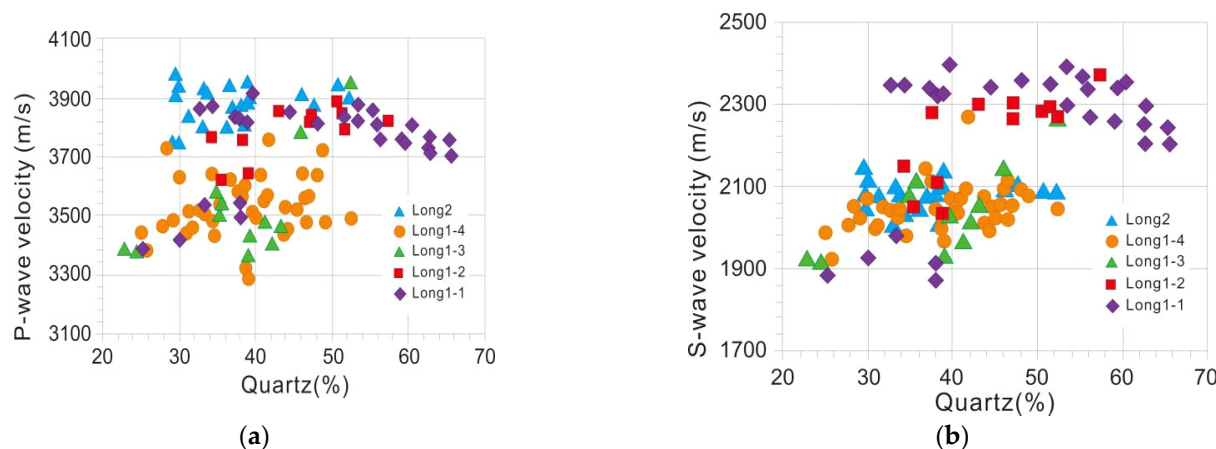


**Figure 7.** P-wave velocity (a) and S-wave velocity (b) as a function of the quartz content of shale samples.

In contrast, the latter results from sorting differences [28]. When the quartz content exceeds 41%, the rock matrix-supported particles gradually vary from clay to quartz particles. At the same time, the acoustic properties of the rock matrix are mainly influenced by rigid quartz particles, increasing the shear velocity of the sample (Figure 7b). In biogenic silica-based samples, the quartz content and TOC, as well as TOC between content and porosity, represent a positive correlation (Figure 6). The TOC and porosity increase together with the quartz content, resulting in the sample showing a trend that the velocity gradually decreases as the quartz content increases. As described above, the organic-rich reservoir (Long 1-1) also contains terrestrial quartz-based samples, clay-supported samples, and quartz particle-backed samples that make the velocity of quartz content vary in an inverted “V” pattern. From the experimental results and analysis mentioned above, it is easy to see that the structural characteristics of the rock matrix are the main factors controlling velocity change, and the porosity and TOC are the secondary characteristics controlling velocity change. The velocity of the quartz content changes the way deep shale samples accord with the speed-varying pattern of mudstone → sandy mudstone → argillaceous sandstone → sandstone, but the porosity evolution is not similar. The difference in porosity variation

indicates that the velocity change in deep shale is not similar to the continuous velocity change in the latter. However, the rock structure as a whole restricts both.

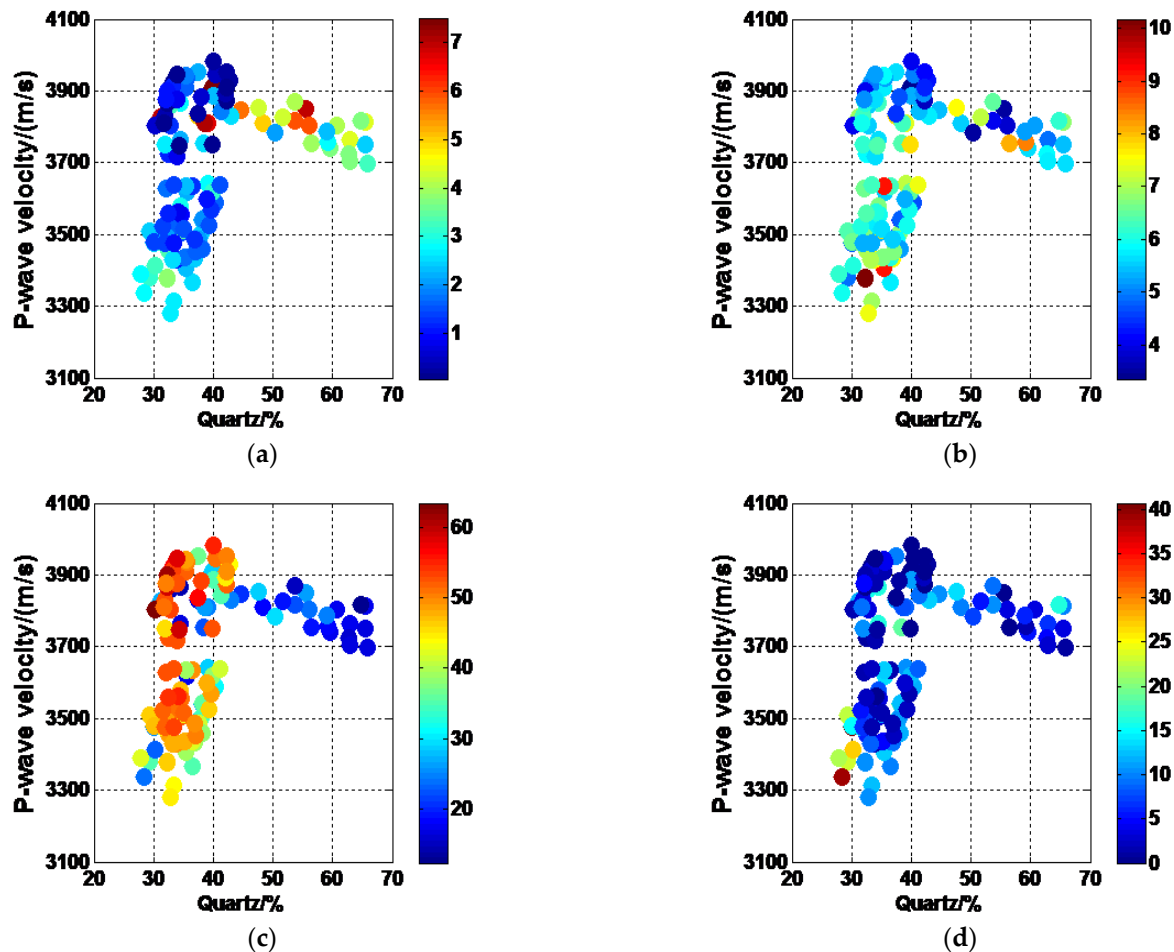


**Figure 8.** Influence of major mineral composition and porosity on the P-wave velocity. Data are sorted by TOC (a), porosity (b), clay content (c), and carbonate content (d).

The dynamic Young modulus ( $E_d$ ) and Poisson's ratio ( $\nu_d$ ) can be calculated using the P-wave and S-wave velocities and densities measured with shale samples [29]:

$$E_d = \frac{\rho V_s^2 (3V_p^2 - 4V_s^2)}{V_p^2 - V_s^2}, \quad (2)$$

$$\nu_d = \frac{V_p^2 - 2V_s^2}{2(V_p^2 - V_s^2)}, \quad (3)$$

where  $V_p$  and  $V_s$  are the P-wave and S-wave velocities in the normal bedding direction, and  $\rho$  is the sample density under dry conditions.

#### 4.3. Variety of Static Mechanical Characteristics of Rock

Rock brittleness is a crucial indicator for assessing a shale reservoir's geomechanical properties and fracture strength [30], with two major methods in logging and brittle seismic evaluation: Young's modulus and Poisson's ratio. The latter indicates the initial fracture strength of the rock under pressure, while the former demonstrates the fracture

maintaining its characteristics. The rock brittleness coefficient defined by elastic parameters is given below [31]:

$$B_1 = \left( \frac{E_d - 1}{14} + \frac{0.4 - v_d}{0.5} \right) \times 100. \quad (4)$$

In the above,  $E_d$  is Young's modulus, unit  $\times 10$  GPa;  $v_d$  is Poisson's ratio. As for the brittleness evaluation method based on rock brittleness and plastic mineral composition, the quartz and dolomite in the shale sample are taken as the main brittle minerals, and the brittleness coefficient defined by mineral composition is shown below [32]:

$$B_2 = \left( V_{quar} + V_{dol} \right) / \left( V_{quar} + V_{dol} + V_{lime} + V_{clay} + V_{TOC} \right), \quad (5)$$

where  $V_{quar}$  and  $V_{dol}$  represent the contents of brittle quartz and dolomite in the sample, and  $V_{lime}$ ,  $V_{clay}$ , and  $V_{TOC}$  stand for the contents of calcite, clay, and TOC in the sample.

Figure 9 provides the sample hardness brittleness index change relationship. The hardness and brittleness indexes  $B_1$  and  $B_2$  show a positive correlation. The organic-rich samples 1-1 exhibit high hardness brittleness values, indicating that available sample hardness represents brittleness change. Because the sample area for the hardness test is small, it is more susceptible to local changes in mineral composition. Moreover, the contribution of minerals, such as calcite, to the brittleness and plasticity of the sample depends on experimental conditions, making the  $B_1$  correlation higher than the  $B_2$  correlation.

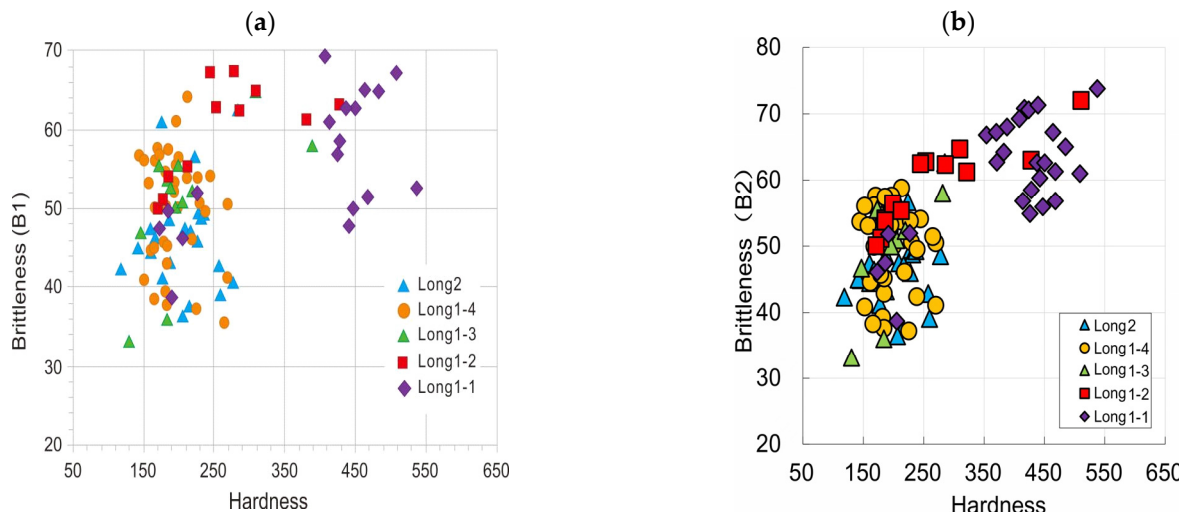


**Figure 9.** Brittleness  $B_1$  (a) and  $B_2$  (b) as a function of the hardness of shale samples.

## 5. Conclusions

- (1) The main mineral composition of the deep shale samples obtained from the Wufeng–Longmaxi Formation in south Sichuan Province is similar to that of the middle-shallow shale in the same layer. Most of the organic-rich shale ( $TOC \geq 2\%$ ) is clay-based siliceous, and the organic-lean shale ( $TOC < 2\%$ ) is chiefly silicon-based grapholith.
- (2) The porosity types of these samples include intergranular, intercrystalline, organic matter, and fracture pores, which are identical to that of shallow shale samples, but the organic matter pores of deep shale samples are less developed. In contrast, the dissolved pores of the deep shale samples increase significantly, forming more pores than in middle-shallow shale samples.
- (3) Organic-rich and organic-lean samples differ significantly in geochemical characteristics. The former is primarily located above the illite Si/Al line, featuring high  $SiO_2$  and low  $Al_2O_3$  and  $TiO_2$ . In addition, it shows a negative correlation with zirconium, which displays that the quartz in the sample originated from early diagenesis (same deposition) of biogenic silicon that allows the sample to be supported by microcrys-

talline quartz grains. Alternatively, a large number of organic-lean reservoir samples are below the illite Si/Al line and feature low  $\text{SiO}_2$  and high  $\text{Al}_2\text{O}_3$  and  $\text{TiO}_2$  and positively correlated with zirconium, indicating that the quartz in the sample is mainly terrestrial clastic quartz that allows the sample to be backed by plastic clay minerals in structure.

- (4) There is a noticeable positive correlation between the shale sample hardness, the brittleness index  $B_1$  calculated using the experiment results of velocity, and the brittleness index  $B_2$  calculated using the mineral composition. The sample hardness (brittleness) is also limited by rock structure, making the hardness (brittleness) change with the quartz content in an asymmetric inverted "V" form. However, it shows a negative relationship with the clay content. Therefore, for organic-lean shale samples with soft clay minerals as rock-supporting particles, an increase in quartz content does not cause the hardness (brittleness) of the sample to vary on a large scale.

**Author Contributions:** Conceptualization, W.G., M.Z., Z.L. and W.S.; Date curation, M.Z., S.Z., P.L. and Y.C.; Funding acquisition, W.G. and W.S.; Investigation, M.Z., S.Z. and P.L.; Resources, M.Z. and Z.L.; Validation, W.G., M.Z., Z.L. and W.S.; Writing—Original draft preparation, W.G., M.Z. and Z.L.; Writing—Review and editing, W.S. All authors have read and agreed to the published version of the manuscript.

**Funding:** This work was supported by the National Natural Science Foundation of China (NO. 12172362), the China National Petroleum Corporation (CNPC) Innovation Found (2021DQ02-0204).

**Data Availability Statement:** Not applicable.

**Conflicts of Interest:** The authors declare no conflict of interest.

## Appendix A

**Table A1.** Database of mineral content and rock physical properties of sales sample at a 40 MPa confining pressure from one hundred and twenty-one plunger samples.

No.	Position	Depth m	Density g/cm <sup>3</sup>	Porosity %	TOC %	Main Mineral Composition %				Hardness	$V_P$ m·s <sup>-1</sup>	$V_S$ m·s <sup>-1</sup>
						Quartz	Clay	Calcite	Dolomite			
1	Long 2	3851.3	2.73	4.2	1.2	50.9	27.1	5.1	1.4	177.0	3947	2089
2	Long 2	3757.6	2.75	4.0	0.9	39.3	45.1	0.0	0.4	168.0	3908	2057
3	Long 1-4	3855.3	2.68	4.5	1.5	48.9	30.8	4.3	0.0	173.7	3717	2073
4	Long 1-4	3782.7	2.63	4.1	2.2	31.9	36.8	3.7	10.8	192.7	3456	2047
5	Long 1-3	3886.0	2.62	6.9	2.4	42.3	26.8	9.3	2.5	186.3	3406	2016
6	Long 1-3	3792.2	2.59	6.4	2.6	39.2	30.2	5.5	3.3	189.0	3366	1932
7	Long 1-2	3890.4	2.66	5.0	2.8	52.6	20.1	6.9	2.3	310.0	3954	2266
8	Long 1-2	3798.4	2.61	4.9	2.1	47.3	20.6	3.2	5.8	245.0	3831	2299
9	Long 1-1	3897.5	2.59	8.4	2.7	59.2	18.2	1.1	0.3	371.3	3756	2255
10	Long 1-1	3804.0	2.52	3.4	7.5	39.8	28.5	0.0	0.0	537.7	3910	2392

Note: TOC content is expressed by mass percent.

## References

- Jia, C.Z.; Zheng, M.; Zhang, Y.F. Unconventional hydrocarbon resources in China and the prospect of exploration and development. *Pet. Explor. Dev.* **2012**, *39*, 129–136. [[CrossRef](#)]
- Shen, W.J.; Li, X.Z.; Ma, T.R.; Cai, J.; Lu, X.; Zhou, S. High-pressure methane adsorption behavior on deep shales: Experiments and modeling. *Phys. Fluids* **2021**, *33*, 063103. [[CrossRef](#)]
- Shen, W.J.; Zuo, L.; Ma, T.R.; Chen, C.; Qin, C.; Yang, L.; Xie, K. Quantitative studies on the characterization and evaluation of adsorbed gas and free gas in deep shale reservoirs. *Energy Fuels* **2023**, *37*, 3752–3759. [[CrossRef](#)]
- Liu, Z.W.; Sa, L.M.; Yang, X.; Li, X.Y. Needs of geophysical technologies for shale gas exploration. *Oil Geophys. Prospect.* **2011**, *46*, 810–818.
- Vernik, L.; Nur, A. Ultrasonic and anisotropy of hydrocarbon source rocks. *Geophysics* **1992**, *57*, 727–735. [[CrossRef](#)]
- Vernik, L.; Liu, X.Z. Velocity anisotropy in shales: A petrophysical study. *Geophysics* **1997**, *62*, 521–532. [[CrossRef](#)]
- Li, X.Y.; Lei, X.L.; Li, Q. Response of velocity anisotropy of shale under isotropic and anisotropic stress fields. *Rock Mech. Rock Eng.* **2018**, *51*, 695–711. [[CrossRef](#)]

8. Sondergeld, C.H.; Rai, C.S.; Margesson, R.W.; Whidden, K. Ultrasonic measurement of anisotropy on the Kimmeridge Shale. In *SEG Expanded Abstracts*; Society of Exploration Geophysicists: Tulsa, OK, USA, 2000; p. 1858.
9. Sondergeld, C.H.; Rai, C.S. Elastic anisotropy of shales. *Lead. Edge* **2011**, *30*, 324–331. [[CrossRef](#)]
10. Dewhurst, D.N.; Siggins, A.F.; Sarout, J.; Raven, M.; Nordgård-Bolås, H.M. Geomechanical and ultrasonic characterization of a norwegian sea shale. *Geophysics* **2011**, *76*, WA101–WA111. [[CrossRef](#)]
11. Deng, J.X.; Wang, H.; Zhou, H.; Liu, Z.H.; Song, L.T.; Wang, X.B. Microtextural, seismic rock physical properties and modeling of Longmaxi Formation shale. *Chin. J. Geophys.* **2015**, *58*, 2123–2136. (In Chinese)
12. Deng, J.X.; Tang, Z.Y.; Li, Y.; Xie, J.; Liu, H.; Guo, W. The influence of the diagenetic process on seismic rock physical properties of Wufeng and Longmaxi Formation shale. *Chin. J. Geophys.* **2018**, *61*, 659–672. (In Chinese)
13. Hornby, B.E.; Schwartz, L.M.; Hudson, J.A. Anisotropic effective-medium modeling of the elastic properties of shales. *Geophysics* **1994**, *59*, 1570–1583. [[CrossRef](#)]
14. Vernik, L.; Milovac, J. Rock physics of organic shales. *Lead. Edge* **2011**, *30*, 324–331. [[CrossRef](#)]
15. Carcione José, M.; Avseth, P. Rock-physics templates for clay-rich source rocks. *Geophysics* **2015**, *80*, D481–D500. [[CrossRef](#)]
16. Guo, Z.Q.; Li, X.Y.; Liu, C.; Feng, X.; Shen, Y. A shale rock physics model for analysis of brittleness index, mineralogy and porosity in the Barnett Shale. *J. Geophys. Eng.* **2013**, *10*, 025006. [[CrossRef](#)]
17. Zhang, F.; Li, X.Y.; Qian, Z. Estimation of anisotropy parameters for shale based on an improved rock physics model. *J. Geophys. Eng.* **2017**, *14*, 143–158. [[CrossRef](#)]
18. Steiger, R.P. Fundamentals and use of potassium/polymer drilling fluids to minimize drilling and completion problems associated with hydratable clays. *J. Pet. Technol.* **1982**, *34*, 1661–1670. [[CrossRef](#)]
19. Shen, W.J.; Ma, T.R.; Li, X.Z.; Sun, B.; Hu, Y.; Xu, J. Fully coupled modeling of two-phase fluid flow and geomechanics in ultra-deep natural gas reservoirs. *Phys. Fluids* **2022**, *34*, 043101. [[CrossRef](#)]
20. Deng, J.; Wang, C.; Zhao, Q.; Guo, W.; Tang, G.; Zhao, J. Depositional and Diagenetic Controls on Macroscopic Acoustic and Geomechanical Behaviors in Wufeng-Longmaxi Formation Shale. *Front. Earth Sci.* **2021**, *9*, 617831. [[CrossRef](#)]
21. Schoenherr, J.; Littke, R.; Urai, J.L.; Kukla, P.A.; Rawahi, Z. Polyphase thermal evolution in the Infra-Cambrian Ara Group (South Oman Salt Basin) as deduced by maturity of solid reservoir bitumen. *Org. Geochem.* **2017**, *38*, 1293–1318.
22. Hickey, J.J.; Bo, H. Lithofacies summary of the Mississippian Barnett Shale, Mitchell 2 TP Sims well, Wise County, Texas. *AAPG Bull.* **2007**, *91*, 437–443. [[CrossRef](#)]
23. Abouelresh, M.O.; Slatt, R.M. Lithofacies and sequence stratigraphy of the Barnett Shale in east-central Fort Worth Basin, Texas. *AAPG Bull.* **2012**, *96*, 1–22. [[CrossRef](#)]
24. Wedepohl, K.H. Environmental influences on the chemical composition of shales and clays. *Phys. Chem. Earth* **1971**, *8*, 307–331. [[CrossRef](#)]
25. Yamamoto, K. Geochemical characteristics and depositional environments of cherts and associated rocks in the franciscan and shimanto terranes. *Sediment. Geol.* **1987**, *52*, 65–108. [[CrossRef](#)]
26. Rowe, H.D.; Loucks, R.G.; Ruppel, S.C.; Rimmer, S.M. Mississippian Barnett Formation, Fort Worth Basin, Texas: Bulk geochemical inferences and Mo-TOC constraints on the severity of hydrographic restriction. *Chem. Geol.* **2008**, *257*, 16–25. [[CrossRef](#)]
27. Ross, D.J.; Bustin, R.M. Investigating the use of sedimentary geochemical proxies for paleoenvironment interpretation of thermally mature organic-rich strata: Examples from the Devonian–Mississippian shales, Western Canadian Sedimentary Basin. *Chem. Geol.* **2009**, *260*, 1–19. [[CrossRef](#)]
28. Avseth, P.; Mukerji, T.; Mavko, G.; Dvorkin, J. Rock-physics diagnostics of depositional texture, diagenetic alterations, and reservoir heterogeneity in high porosity siliciclastic sediments and rocks—A review of selected models and suggested work flows. *Geophysics* **2010**, *75*, 31–147. [[CrossRef](#)]
29. Mavko, G.; Mukerji, T.; Dvorkin, J. *The Rock Physics Handbook*, 2nd ed.; Cambridge University Press: Cambridge, UK, 2009.
30. Li, Q.H.; Chen, M.; Jin, Y.; Wang, F.P.; Hou, B.; Zhang, B.W. Indoor evaluation method for shale brittleness and improvement. *Chin. J. Rock Mech. Eng.* **2012**, *31*, 1680–1686. (In Chinese)
31. Rickman, R.; Mullen, M.; Petre, J.E.; Grieser, W.V.; Kundert, D. A practical use of shale petrophysics for stimulation design optimization: All shale plays are not clones of the barnett shale. In Proceedings of the SPE Annual Technical Conference and Exhibition, Denver, CO, USA, 21–24 September 2008; p. 115258.
32. Wang, F.P.; Gale, J.F.W. Screening criteria for shale-gas systems. *Trans. Gulf Coast Assoc. Geol. Soc.* **2009**, *59*, 779–793.

**Disclaimer/Publisher's Note:** The statements, opinions and data contained in all publications are solely those of the individual author(s) and contributor(s) and not of MDPI and/or the editor(s). MDPI and/or the editor(s) disclaim responsibility for any injury to people or property resulting from any ideas, methods, instructions or products referred to in the content.